PAPER

Can armchair nanotubes host organic color centers?

To cite this article: Benjamin Eller et al 2022 J. Phys.: Condens. Matter 34 464004

View the <u>article online</u> for updates and enhancements.

You may also like

- Thermoelectric transport properties of XAgP (X = Sr and Ba) from first principles Rakshanda Dhawan, Mohd Zeeshan, Tashi Nautiyal et al.
- DFT-1/2 method applied to 3D topological insulators
 Tulio Mota, Filipe Matusalem, Marcelo Marques et al.
- Kinetics of inherent processes counteracting crystallization in supercooled monatomic liquid B N Galimzyanov, D T Yarullin and A V Mokshin

Can armchair nanotubes host organic color centers?

Benjamin Eller^{1,*}, Jacob Fortner^{1,2}, Jacek Kłos³, YuHuang Wang^{1,2,*} and Charles W Clark^{3,4,*}

E-mail: beller@umd.edu, yhw@umd.edu and charles.winthrop.clark@gmail.com

Received 31 May 2022, revised 15 August 2022 Accepted for publication 5 September 2022 Published 27 September 2022



Abstract

We use time-dependent density functional theory to investigate the possibility of hosting organic color centers in (6, 6) armchair single-walled carbon nanotubes, which are known to be metallic. Our calculations show that in short segments of (6, 6) nanotubes ~ 5 nm in length there is a dipole-allowed singlet transition related to the quantum confinement of charge carriers in the smaller segments. The introduction of sp^3 defects to the surface of (6, 6) nanotubes results in new dipole-allowed excited states. Some of these states are redshifted from the native confinement state of the defect-free (6, 6) segments; this is similar behavior to what is observed with sp^3 defects to exciton transitions in semiconducting carbon nanotubes. This result suggests the possibility of electrically wiring organic color centers directly through armchair carbon nanotube hosts.

1

Supplementary material for this article is available online

Keywords: defect luminescence, armchair nanotubes, metallic nanomaterials, organic color center, Pople basis set

(Some figures may appear in colour only in the online journal)

Organic color centers (OCCs) are room-temperature sources of single-photons enabled by organic, fluorescent sp^3 defects that are covalently functionalized on semiconducting single-walled carbon nanotubes (CNTs) [1–12] (examples depicted in figure 1). The defect photoluminescence (E_{11}^-) redshifts from the E_{11} excitonic photoluminescence intrinsic to the defect-free CNT hosts, due to the local perturbation of the fundamental chemical and geometric structure of the CNT by the introduction of the defect. OCCs feature intriguing physics and chemistry, including exciton trapping and up-conversion, dark

exciton brightening and molecular tunability, which hold substantial potential for sensing, imaging and quantum information science applications [9].

So far OCCs have only been synthesized on semiconducting CNTs. However, it is an intriguing question whether OCCs can be hosted on metallic CNTs such that the color centers are directly wired to CNT electrodes. An OCC hosted on a metallic nanotube would effectively make electrical contacts directly to the color center. Electroluminescence of OCCs has been previously demonstrated from OCCs in semiconducting CNT hosts [12]. Since metallic CNTs exhibit an Ohmic response to applied voltages OCC emission could be driven with low currents. The low currents should also result in

¹ Chemical Physics Program, University of Maryland, College Park, MD 20742, United States of America

² Department of Chemistry & Biochemistry, University of Maryland, College Park, MD 20742, United States of America

³ Joint Quantum Institute, Department of Physics, University of Maryland, College Park, MD 20742, United States of America

⁴ National Institute of Standards and Technology and the University of Maryland, Gaithersburg, MD 20899, United States of America

^{*} Authors to whom any correspondence should be addressed.

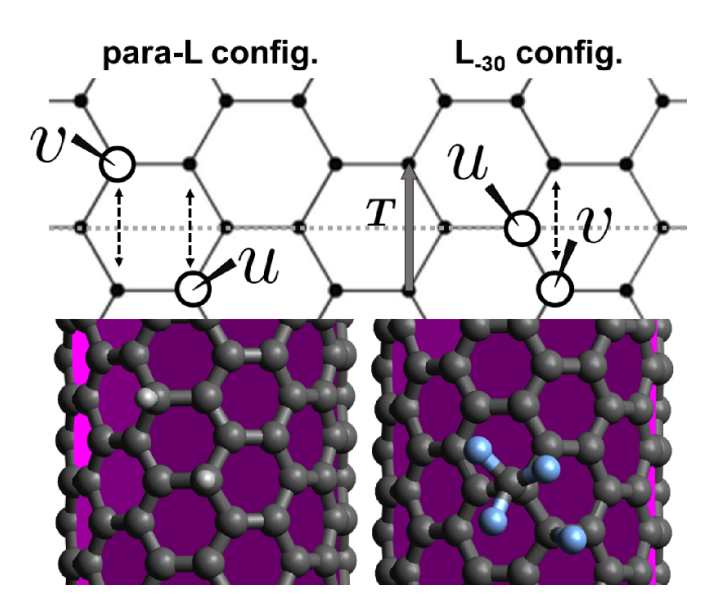


Figure 1. (Above) The two defect configurations of defect complexes (u, v, w) considered for (6, 6) CNTs in this paper, the $w = L_{-30}$ configuration and the w = para-L configuration. The translation vector of the (6, 6) CNT is T. Example molecular models for the two configurations are shown below, for the specific defects (H, H, para-L) (left) and $(\text{CF}_3, F, L_{-30})$ (right). (Below) Close-up of optimized structures of (6, 6) models with defects, visualized with Avogadro molecular editing software [13].

relatively low power dissipation which would be advantageous for device incorporation by limiting the impact of heating effects. However, it is well known that fluorescence quenching occurs when molecules are in contact with metals which begs the question of whether OCCs can be hosted on metallic nanotubes at all.

Excitons-strongly correlated states of electrons and holes—are essential to understanding the optical properties of CNTs [14], and the OCC fluorescence in semiconducting CNTs is linked to trapping an exciton at the defect site [3]. In a metal it is expected that the screening of the hole from an excited electron diminishes the Coulomb attraction between them and precludes exciton states. However, this screening effect is reduced in CNTs due to their effective 1D nature [15]. First principles methods based on the GW approximation to the electron self-energy and the Bethe-Salpeter equation predict the existence of a sole bound exciton state in (3,3)armchair metallic CNTs, which is supported by subsequent experiments [15, 16]. The existence of a bound exciton state in metallic CNTs is understood as being due to the interaction potential between the electron and hole being a Dirac δ function of their relative displacement, since a 1D δ -function potential well $V(x) = -V_0 a \delta(x)$ supports a single localized eigenstate $\psi(x) = \sqrt{\kappa}e^{-\kappa|x|}$ (with $V_0a > 0$ and κ related to the eigenenergy). Thus, the unconventional metallic properties granted by the reduced dimensionality allow for the possibility of directly embedding an OCC on metallic CNTs.

To determine whether armchair CNTs host OCCs we performed time-dependent density functional theory (TDDFT) calculations on DFT geometry-optimized (6,6) CNT models. We studied models of different lengths L with and without

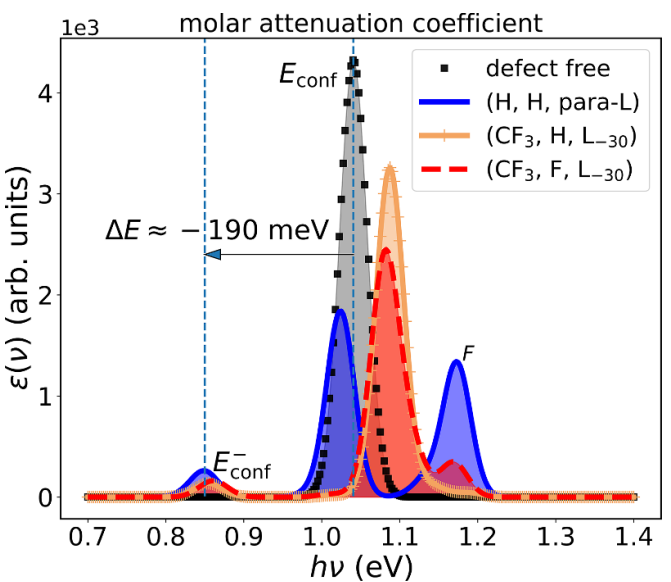


Figure 2. Calculated molar attenuation coefficient spectra for (6,6) CNTs with L=17, for a (H, H, para-L) defect (blue solid-line), a (CF₃, H, L₃₀) defect (tan plus-line), and a (CF₃, F, L₃₀) (red dashed-line) defect compared against the same defect-free segment (black squares). Note that each defect-laden CNT has a feature at around 0.85 eV, and the colors of the spectra are merely for contrast.

 sp^3 defects defined near the center of the model, with L being the number of unit cells. The calculations provide information about the electronic ground and low-lying excited states of the segments, such as optimized ground state structure and excited state energies and oscillator strengths f_n , which are a measure of the likelihood the system decays to the ground state by photoemission (or excites from the ground state through photoabsorption, as the case may be).

The results of our calculations show that due to quantum confinement of the excited conduction electron and valence hole in short segments of (6, 6) nanotubes ~5 nm, there is a dipole-allowed singlet transition. Furthermore, our calculations also show that the introduction of certain sp^3 defects to the center of the (6, 6) segments leads to new opticallyallowed $(f_n > 0)$ transitions between singlet excited states and the ground state. In particular for ≈4.25 nm long segments (L=17), all three defect group pairs (H, H, para-L), (CF_3, H, L_{-30}) and (CF_3, F, L_{-30}) introduce singlet states with excitation energies close to 0.85 eV with oscillator strengths \sim 1/10 of the initial $E_{\rm conf}$ value. As indicated in figure 2, these states are lower in energy than the native $E_{\rm conf}$ state by an amount comparable to shifts seen in experiment [9], and no such state exists in the corresponding defect free L = 17 segment. This combined with further analysis leads us to hypothesize that it is indeed possible to create OCCs in armchair metallic CNTs, which would provide a new platform in which to study excitonic and potentially trionic physics in the presence of OCCs and a stepping-stone towards deterministic creation of a single-photon via electroluminescence.

Our calculations were performed using the B3LYP approximation for the exchange-correlation energy functional [17–20] with a 6-31g Pople basis set [21], using the DFT

methods implemented in Gaussian v16 [22]. First, we generated molecular models of (6,6) CNT segments composed of L unit cells with TubeGen [23] and saturated the bonds of the terminal C atoms with H atoms. Next, we performed DFT geometry optimization calculations, obtaining the ground state Kohn-Sham orbitals and energies. Structurally optimized CNTs were used to define the electronic ground state for subsequent TDDFT calculations, obtaining the first ten singlet and ten triplet excited states. This provided the oscillator strengths f_n for the transitions between excited states n and the ground state, a measure of the likelihood of the transition being radiative and leading to emission/absorption of a photon [24, 25]. Having the f_n for the excited states from our TDDFT calculations, we calculated the molar attenuation coefficient for the relevant range of frequencies (only the singlet states have non-zero f_n). The results are shown in figure 2 for CNT segments with L = 17. We performed these calculations first with defect-free models, then for segments with one of three sp^3 defects defined near the center of the CNT (example model shown in figure 1). Each defect is labeled as (u, v, w), where u and v are chemical/atomic species that lack any bonding character with each other, termed a monovalent [10] defect, and w refers to a specific bonding configuration of u and v with the CNT. The defects we studied were (CF₃, H, L_{-30}), (H, H, para-L) and (CF_3, F, L_{-30}) . The terminology for configurations follows [10] for L_{-30} and [26] for para-L, and these configurations are illustrated in figure 1 for (6, 6) CNTs. We note that the configurational nature of a defect affects the optical properties of the resulting OCC and samples produced of CNTs with OCCs typically have a mixture of configurations [1, 5, 7, 9, 27–31], although it was recently shown that this can be controlled with laser irradiation [32]. In this work we consider configurations w that are farthest in symmetry from the defect-free (6, 6) segments, i.e. for which the positions of the defects' atomic constituents changed the most under the action of reflection through the bisecting plane indicated by the horizontal dotted line in figure 1.

We will begin by considering what happens to the frequency-dependent molar attenuation coefficient $\varepsilon(\nu)$ of (6,6) CNT segments in the optical-NIR range when certain sp^3 defects are introduced to the surface. Density functional theory calculations by Kilina $et\ al$ have shown that various sp^3 defects bound to sidewalls of semiconducting CNTs result in new peaks in calculated absorption spectra which are redshifted from, or lower in energy than the native E_{11} peak [26]. In experiments on semiconducting CNTs with OCCs it is found that the photoluminescence emission peak from the OCCs is redshifted from the less intense native E_{11} peak by nearly 200 meV, depending on the specific CNT and defect [1].

This new dipole-allowed defect state is lower in energy than the dark exciton states of the CNT [33–37], offering a radiative decay route to brighten the dark excitons [1]. Inspired by these observations in semiconductors, we use TDDFT to calculate the low-energy electronic excited states of armchair (6,6) CNT models aimed at finding their counterparts in metallic hosts. We modeled three different sp^3 defects and use the predicted oscillator strengths of these states to obtain the molar

attenuation coefficients versus energy. We compare the coefficient calculated for a defect free segment to those where an sp^3 defect is defined near the center of the CNT. Information about the defects and how they are labeled is provided in figure 1 and Methods, while the attenuation coefficients are shown in figure 2 for (6, 6) segments with L = 17.

We can make a few observations about figure 2. First, for each CNT with a defect, there is a peak located near $h\nu=0.85$ eV of minor but not negligible oscillator strength. There is no corresponding feature in the spectrum for the defect-free CNT. Furthermore, these new peaks are lower in energy than the $E_{\rm conf}$ peak by about 0.19 eV, which is comparable to the redshifts seen in experiments between the E_{11} and E_{11}^- , as well as several of the shifts seen in calculations on semiconducting CNTs with sp^3 defects [1, 9, 26]. The central 4 peaks all can be traced to the $E_{\rm conf}$ label for the defect-free CNT. Also note the additional features labelled F in figure 2 which are only present for the segments with (H, H, para-L) and (CF₃, F, L₃₀) defects.

We note that the $E_{\rm conf}$ peak in figure 2 is not the E_{11} transition between van Hove singularities of the (6, 6) CNT, which has an energy around 2.71 eV [38]. $E_{\rm conf}$ arises from quantum confinement of the electron and hole in shorter CNT segments. This confinement effect can be seen in figure 4, where we plot the $E_{\rm conf}$ peak values for defect-free (6, 6) segments of different L and see that the energy of this transition, and thus the excited state of the carriers, increases as we squeeze them into smaller L CNTs. The finite size leads to the $E_{\rm conf}$ transition, and the sp^3 defects peel off oscillator strength from this to a redshifted singlet transition in a manner analogous to the behavior of the E_{11} and E_{11}^- transitions in semiconducting CNTs with OCCs (sp^3) defects).

The calculated single-particle energy gaps for defect-free (6,6) CNTs are obtained from the ground-state optimization and plotted for segments of different L in figure 4. We see an overall decreasing trend in the HOMO-LUMO gap as a function of L, a decay with a characteristic oscillatory behavior with period 3. A similar oscillatory behavior seen with DFT calculations on graphene nanoribbons was reported in [39] where they explain this effect as originating from the fact that the Fermi wavelength of graphene is about 3 unit cells of the armchair CNTs (or equivalently, zigzag nanoribbons). The graphene nanoribbon systems can be mapped onto finite segments of CNTs, which aside from effects due to the nonzero curvature of the nanotubes that result in a shift to the computed Kohn-Sham eigenenergies explains the trends we observe here.

The HOMO–LUMO gap is simply the molecular limit of [6] CPP [40], corresponding to unit cells. Our excited state calculations reproduce the absortion peak observed experimentally [40], with our absorption peak blueshifted from the measured [6] CPP peak of 338 nm by about 16 nm, which lends a degree of support to our small L results. Thus, our ground-state calculations produce results that are qualitatively correct in behavior with increasing L, and reasonably reproduce the wavelength of the experimentally measured absorption peak for the smallest considered 'segment'. We envision experimental verification may be achievable through a combination

of lithography and chemistry for the creation of single defects in ultrashort channels [41, 42].

To obtain more insight into the nature of the different features in the spectra plotted in figure 2 we consider the single-particle Kohn–Sham orbital compositions of the relevant excited states, which are provided as output of our TDDFT calculations. Let ψ_0', ψ_1', \ldots refer to the LUMO, the next highest molecular orbital LUMO+1 and so on, and $\psi_0, \psi_{-1}, \ldots$ refer to the HOMO, next lowest HOMO-1, etc. Each singly-excited state n can be thought of as a combination of particle-hole amplitudes

$$\Psi_n(\mathbf{r}_e, \mathbf{r}_h) = \sum_{ia} c_{ia}[n] \psi_i(\mathbf{r}_h) \psi_a'(\mathbf{r}_e)$$
 (1)

where the electrons are viewed as being excited to particle orbitals in the virtual (ground-state unoccupied) manifold and the holes are left behind as orbitals in the occupied manifold, and different pairs can contribute different amounts to the overall transition described by the set of $c_{ia}[n]$. The orbital characterizations of various excited states are listed in table 1, and isosurfaces of dominant-contributing orbitals for defect-free and defect-containing (6,6) CNT models are presented in the supplemental data for comparison, along with orbitals from semiconducting (6,5) models with the same defect.

For the defect-free segment in figure 2 there is one radiative transition in the energy range considered, labelled $E_{\rm conf}$, which has an orbital composition mostly given by $(0.52536\psi_{-1}\psi_0' - 0.50489\psi_0\psi_1')$, or equal parts HOMO-1—LUMO and HOMO—LUMO+1. In the presence of the defect, the orbital composition of the other three central peaks contains major contributions from an $(a\psi_{-1}\psi_0' - b\psi_0\psi_1')$ term like the one that dominates the $E_{\rm conf}$ feature, along with additional $\psi_{-1}\psi_1'$ contributions.

Let us compare the orbital composition of the $E_{\rm conf}$ peak to those of the new features seen in the spectra for the L=17 CNTs with defects. First consider the peak labeled by $E_{\rm conf}^-$, which is present for all three defects. Looking at the orbital compositions in table 1, we see that each one contains again a contribution of the form $(a\psi_{-1}\psi_0'-b\psi_0\psi_1')$ like the radiative $E_{\rm conf}$ transitions (though the orbitals are specific to a given system). For the L=17 CNTs with (CF₃, F, L₋₃₀) the $E_{\rm conf}^-$ feature is actually composed of two excited states close in energy and oscillator strength, and the overall orbital characterizations involve a greater number of orbitals. We will refer to the lower energy state of the pair as $E_{\rm conf}^{-,r}$ and the higher energy state of the pair as $E_{\rm conf}^{-,r}$. Each of these states has a similar contribution from the $(a\psi_{-1}\psi_0'-b\psi_0\psi_1')$ terms. The E_{11}^{-} feature appears to thus be similar in nature to the E_{11} , except with an additional major contribution from a $\psi_{-1}\psi_1'$ pair and in the cases of $E_{-}^{-,r}$, and $E_{-}^{-,b}$ from $\psi_{-2}\psi_0'$

in the cases of $E_{\rm conf}^{-,r}$ and $E_{\rm conf}^{-,b}$ from $\psi_{-2}\psi_0'$. To better understand why only two defects have states in their $\varepsilon(\nu)$ associated with the F feature while all possess $E_{\rm conf}^{-}$ associated absorption, we examined the symmetry of these defect-tailored structures. A lone sp^3 defect on a CNT surface breaks various symmetries present in the armchair CNT, depending on the geometry of the defect. We can see which

Table 1. Table presenting orbital descriptions of several transitions from figure 2. The double parentheses indicate a contribution of the form $(a\psi_{-1}\psi_0'-b\psi_0\psi_1')$. Visual representations of key orbitals are shown in the supplemental data.

$\varepsilon(\nu)$ peak	Orbital description	f_n
	L = 17 defect-free	
$E_{\rm conf} (1.04 \mathrm{eV})$	$((0.53\psi_{-1}\psi_0' - 0.51\psi_0\psi_1'))$	6.4
	L = 17 (H, H, para-L)	
$E_{\rm conf}$ (1.02 eV)	$((-0.37\psi_{-1}\psi'_0 + 0.35\psi_0\psi'_1)) + 0.37\psi_{-1}\psi'_1 - 0.21\psi_{-1}\psi'_2 + 0.13\psi_0\psi'_0 - 0.19\psi_0\psi'_3$	2.7
$E_{\rm conf}^- (0.850 {\rm eV})$	$((0.27\psi_{-1}\psi'_0 - 0.24\psi_0\psi'_1)) + 0.58\psi_{-1}\psi'_1 + 0.13\psi_0\psi'_2$	0.38
F (1.17 eV)	$0.37\psi_{-3}\psi'_0 + 0.30\psi_{-2}\psi'_1 ((-0.17\psi_{-1}\psi'_0 + 0.17\psi_0\psi'_1)) + 0.39\psi_{-1}\psi'_2 + 0.16\psi_0\psi'_3$	2.0
F' (1.14 eV)	$-0.36\psi_{-1}\psi_{2} + 0.16\psi_{0}\psi_{3}$ $-0.36\psi_{-3}\psi_{0}' + 0.26\psi_{-2}\psi_{1}'$ $-0.15\psi_{-1}\psi_{2}' + 0.50\psi_{0}\psi_{3}'$ $-0.12\psi_{-1}\psi_{0}'$	0.28
	$L = 17 (CF_3, H, L_{-30})$	
$E_{\rm conf}$ (1.09 eV)	$\begin{array}{l} ((0.39\psi_{-1}\psi_0' - 0.39\psi_0\psi_1')) \\ -0.17\psi_{-2}\psi_1' + 0.31\psi_{-1}\psi_1' \\ +0.15\psi_0\psi_0' - 0.23\psi_0\psi_3' \end{array}$	4.1
E_conf (0.854 eV)	$((-0.23\psi_{-1}\psi_0' + 0.23\psi_0\psi_1')) + 0.61\psi_{-1}\psi_1'$	0.21
	$L = 17 (CF_3, F, L_{-30})$	
$E_{\rm conf} (1.08 \rm eV)$	$\begin{array}{l} ((-0.36\psi_{-1}\psi_0' + 0.36\psi_0\psi_1')) \\ +0.19\psi_{-3}\psi_0' - 0.13\psi_{-2}\psi_2' \\ -0.34\psi_{-1}\psi_1' + 0.14\psi_{-1}\psi_3' \\ -0.16\psi_0\psi_0' - 0.13\psi_0\psi_3' \end{array}$	3.5
$E_{\rm conf}^{-,r}$ (0.856 eV)	$\begin{array}{l} ((-0.18\psi_{-1}\psi_0' + 0.21\psi_0\psi_1')) \\ + -0.36\psi_{-2}\psi_0' + 0.42\psi_{-1}\psi_1' \\ + 0.11\psi_{-1}\psi_2' + 0.27\psi_0\psi_2' \\ -0.10\psi_0\psi_3' \end{array}$	0.13
$E_{\rm conf}^{-,b}$ (0.866 eV)	$((-0.16\psi_{-1}\psi_0' + 0.17\psi_0\psi_1')) +0.35\psi_{-2}\psi_0' + 0.42\psi_{-1}\psi_1' -0.15\psi_{-1}\psi_2' - 0.31\psi_0\psi_2'$	0.13
F (1.17 eV)	$-0.22\psi_{-4}\psi'_0 + 0.61\psi_{-2}\psi'_2$ $-0.12\psi_{-2}\psi'_3 - 0.10\psi_0\psi'_0$ $+0.13\psi_0\psi'_4 - 0.13\psi_0\psi'_5$	0.52
F' (1.11 eV)	$-0.30\psi_{-3}\psi_0' + 0.17\psi_{-2}\psi_1' +((-0.14\psi_{-1}\psi_0' + 0.14\psi_0\psi_1')) +0.40\psi_{-1}\psi_2' - 0.18\psi_{-1}\psi_3' +0.34\psi_0\psi_3'$	0.72

symmetries the different defects we consider break by referring to figures 1 and 3. The defect-free (6,6) CNT possesses C_2 , C_3 and C_6 rotational symmetry about the CNT axis, as well as inversion symmetry and mirror symmetry [43] through a plane perpendicular to the tube axis, as indicated by the horizontal dotted line in figure 1. A single defect of any variety breaks all rotational symmetry about the CNT axis. Somewhat more subtly, all defects we consider break mirror symmetry in the system, as well as inversion symmetry. Why then do

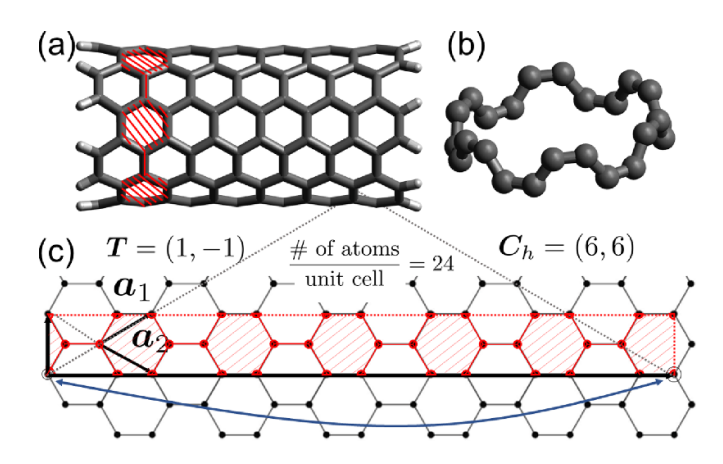


Figure 3. A depiction of (a) (6,6) molecular model with L=7, as well as (c) the underlying geometry defined on a 2D graphene layer, with the lattice vectors a_1, a_2 . For CNTs with chiral vector (which wraps around the circumference of the nanotube)

 $C_h = 6a_1 + 6a_2 = (6,6)$, the translation symmetry vector along the length of the nanotube is T = (1,-1), defining the unit cell shown in red. A unit cell equivalent to the cell highlighted in red in (c) that is used for the computational models is shown in (b).

we see that two of our defects lead to a state at F in figure 2 while the third does not? Consider a (CF₃, F, L₋₃₀) defect and a (CF_3, H, L_{-30}) defect. The CF_3 constituent respects the mirror symmetry in the ground state. While the H-adjunct in (CF₃, H, L₋₃₀) breaks the mirror symmetry, in terms of the local electronic structure the H atom is a small perturbation and should mostly serve to terminate the bond introduced by the CF₃. The F-adjunct represents a more significant alteration of the local electron density, as F brings in nine new electrons instead of one. One electron should serve to satisfy the bond with the C in the CNT while the remaining eight will contribute to new properties and behavior. In particular, it should be expected that the F-adjunct will perturb more the position of the neighboring CF₃ from its symmetric orientation than the H-adjunct. The combination of the two defects is important, and the (H, H, para-L) defect is different in this respect as well as its configuration than the other two defect pairs considered in this work. In other words, the (CF_3, H, L_{-30}) defect nearly retains the mirror symmetry through the plane indicated with a dotted line in figure 1, while both the (CF₃, F, L₋₃₀) and (H, H, para-L) break it. The keyword is nearly, which relates to the fact that there exists such an F state for (CF₃, H, L_{-30}), but it has a negligible oscillator strength compared to those for the other defects.

In conclusion, we have used TDDFT calculations to gain insight into how sp^3 defects affect the optical properties of metallic CNTs. The results of our calculations show that in short segments of (6, 6) nanotubes ~ 5 nm in length there is a dipole-allowed singlet transition related to the quantum confinement of charge carriers. Upon the introduction of different sp^3 defects to the surface of (6, 6) CNTs there arise new excited states that take oscillator strength away from this confinement-related transition. In particular, all defects studied in this work introduce a state lower in energy than this $E_{\rm conf}$ state responsible for the emission observed in the defect-free

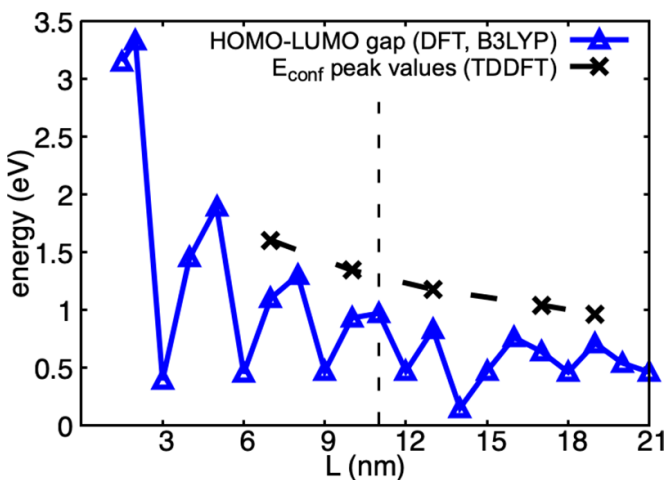


Figure 4. Ground-state HOMO-LUMO energy gaps and $E_{\rm conf}$ values from TDDFT for defect-free (6,6) CNTs as a function of unit cells L. Based on our optimized geometries, there are about (17/4) unit cells per nm. Using this conversion, the distance around our (6,6) segment circumference is indicated as the vertical line at L=11. As the length of the finite segments is decreased and the excited carriers are confined in a smaller space, the energy of the first absorption peak in the defect-free (6,6) increases. This tracks with the increase in HOMO-LUMO gap as L is decreased, and with its decay as L gets larger.

scenario. These states are roughly 0.19 eV lower in energy than the $E_{\rm conf}$, comparable to what is experimentally observed for redshifts between E_{11} and E_{11}^- excitonic transitions in semi-conducting CNTs with sp^3 defects. Depending on the specific nature of the sp^3 defect in the (6, 6) segments, different states can be turned off and on, and the breaking of the (6, 6) CNT symmetries by the defect is likely responsible for which states are introduced. This suggests the possibility of wiring organic color centers with armchair carbon nanotubes.

Data availability statement

All data that support the findings of this study are included within the article (and any supplementary files).

Acknowledgments

This material is based upon work supported by the National Science Foundation under Award No. 1839165. We would like to acknowledge the Alexander Family for their generous support through the Alexander Family Fellowship for students of the Chemical Physics Program at the University of Maryland. Also, we thank the Maryland Advanced Research Computing Center (MARCC) for providing the computing resources needed to complete this work.

ORCID iDs

Benjamin Eller https://orcid.org/0000-0002-6538-4768 Jacek Kłos https://orcid.org/0000-0002-7407-303X YuHuang Wang https://orcid.org/0000-0002-5664-1849

References

- [1] Piao Y, Meany B, Powell L R, Valley N, Kwon H, Schatz G C and Wang Y 2013 Brightening of carbon nanotube photoluminescence through the incorporation of sp³ defects Nat. Chem. 5 840
- [2] Brozena A H, Leeds J D, Zhang Y, Fourkas J T and Wang Y 2014 Controlled defects in semiconducting carbon nanotubes promote efficient generation and luminescence of trions ACS Nano 8 4239
- [3] Kwon H, Furmanchuk A, Kim M, Meany B, Guo Y, Schatz G C and Wang Y 2016 Molecularly tunable fluorescent quantum defects J. Am. Chem. Soc. 138 6878
- [4] He X et al 2017 Tunable room-temperature single-photon emission at telecom wavelengths from sp³ defects in carbon nanotubes Nat. Photon. 11 577–82
- [5] He X et al 2017 Low-temperature single carbon nanotube spectroscopy of sp³ quantum defects ACS Nano 11 10785
- [6] Srinivasan K and Zheng M 2017 Nanotube chemistry tunes light Nat. Photon. 11 535–7
- [7] Wu X, Kim M, Kwon H and Wang Y 2018 Photochemical creation of fluorescent quantum defects in semiconducting carbon nanotube hosts Angew. Chem., Int. Ed. 57 648
- [8] Danné N et al 2018 Ultrashort carbon nanotubes that fluoresce brightly in the near-infrared ACS Nano 12 6059
- [9] Brozena A H, Kim M, Powell L R and Wang Y 2019 Controlling the optical properties of carbon nanotubes with organic colour-centre quantum defects *Nat. Rev. Chem.* 3 375
- [10] Gifford B J et al 2019 Optical effects of divalent functionalization of carbon nanotubes Chem. Mater. 31 6950
- [11] Kwon H et al 2019 Probing trions at chemically tailored trapping defects ACS Cent. Sci. 5 1786–94
- [12] Xu B, Wu X, Kim M, Wang P and Wang Y 2021 Electroluminescence from 4-nitroaryl organic color centers in semiconducting single-wall carbon nanotubes *J. Appl. Phys.* 129 044305
- [13] Hanwell M D, Curtis D E, Lonie D C, Vandermeersch T, Zurek E and Hutchison G R 2012 Avogadro: an advanced semantic chemical editor, visualization and analysis platform J. Cheminform. 4 17
- [14] Wang F, Dukovic G, Brus L E and Heinz T F 2005 The optical resonances in carbon nanotubes arise from excitons *Science* 308 838–41
- [15] Spataru C D, Ismail-Beigi S, Benedict L X and Louie S G 2004 Excitonic effects and optical spectra of single-walled carbon nanotubes *Phys. Rev. Lett.* 92 077402
- [16] Wang F, Cho D J, Kessler B, Deslippe J, Schuck P J, Louie S G, Zettl A, Heinz T F and Shen Y R 2007 Observation of excitons in one-dimensional metallic single-walled carbon nanotubes *Phys. Rev. Lett.* 99 227401
- [17] Becke A D 1993 Density-functional thermochemistry. III. The role of exact exchange *J. Chem. Phys.* **98** 5648
- [18] Lee C, Yang W and Parr R G 1988 Development of the Colle-Salvetti correlation-energy formula into a functional of the electron density *Phys. Rev.* B 37 785
- [19] Vosko S H, Wilk L and Nusair M 1980 Accurate spin-dependent electron liquid correlation energies for local spin density calculations: a critical analysis *Can. J. Phys.* 58 1200
- [20] Stephens P J, Devlin F J, Chabalowski C F and Frisch M J 1994 Ab initio calculation of vibrational absorption and circular dichroism spectra using density functional force fields J. Phys. Chem. 98 11623

- [21] Hehre W J, Ditchfield R and Pople J A 1972 Self-consistent molecular orbital methods. XII. Further extensions of Gaussian-type basis sets for use in molecular orbital studies of organic molecules J. Chem. Phys. 56 2257
- [22] Frisch M J et al 2016 Gaussian 16 Revision B.01 (Wallingford, CT: Gaussian Inc.) (available at: https://gaussian.com/citation/)
- [23] Frey J T and Doren D J 2011 Tubegen 3.4 (web-interface) (available at: http://turin.nss.udel.edu/research/ tubegenonline.html)
- [24] Bethe H A and Salpeter E E 1957 Quantum Mechanics of Oneand Two-Electron Atoms (New York: Academic Press)
- [25] Fano U and Cooper J W 1968 Spectral distribution of atomic oscillator strengths Rev. Mod. Phys. 40 441
- [26] Kilina S, Ramirez J and Tretiak S 2012 Brightening of the lowest exciton in carbon nanotubes via chemical functionalization *Nano Lett.* 12 2306
- [27] Luo H-B, Wang P, Wu X, Qu H, Ren X and Wang Y 2019 One-pot, large-scale synthesis of organic color center-tailored semiconducting carbon nanotubes ACS Nano 13 8417
- [28] He X, Sun L, Gifford B J, Tretiak S, Piryatinski A, Li X, Htoon H and Doorn S K 2019 Intrinsic limits of defect-state photoluminescence dynamics in functionalized carbon nanotubes *Nanoscale* 11 9125
- [29] Berger F J et al 2019 Brightening of long, polymer-wrapped carbon nanotubes by sp³ functionalization in organic solvents ACS Nano 13 9259
- [30] Powell L R, Piao Y and Wang Y 2016 Optical excitation of carbon nanotubes drives localized diazonium reactions J. Phys. Chem. Lett. 7 3690
- [31] Shiraki T, Miyauchi Y, Matsuda K and Nakashima N 2020 Carbon nanotube photoluminescence modulation by local chemical and supramolecular chemical functionalization Acc. Chem. Res. 53 1846
- [32] Qu H, Wu X, Fortner J, Kim M, Wang P and Wang Y 2022 Reconfiguring organic color centers on the sp² carbon lattice of single-walled carbon nanotubes ACS Nano 16 2077–87
- [33] Zhao H and Mazumdar S 2004 Electron-electron interaction effects on the optical excitations of semiconducting single-walled carbon nanotubes *Phys. Rev. Lett.* 93 157402
- [34] Spataru C D, Ismail-Beigi S, Capaz R B and Louie S G 2005 Theory and *ab initio* calculation of radiative lifetime of excitons in semiconducting carbon nanotubes *Phys. Rev. Lett.* **95** 247402
- [35] Capaz R B, Spataru C D, Ismail-Beigi S and Louie S G 2006 Diameter and chirality dependence of exciton properties in carbon nanotubes *Phys. Rev.* B 74 121401(R)
- [36] Ando T 2006 Effects of valley mixing and exchange on excitons in carbon nanotubes with Aharonov-Bohm flux J. Phys. Soc. Japan 75 024707
- [37] Scholes G D, Tretiak S, McDonald T J, Metzger W K, Engtrakul C, Rumbles G and Heben M J 2007 Low-lying exciton states determine the photophysics of semiconducting single wall carbon nanotubes J. Phys. Chem. C 111 11139–49
- [38] Hároz E H, Duque J G, Tu X, Zheng M, Hight Walker A R, Hauge R H, Doorn S K and Kono J 2013 Fundamental optical processes in armchair carbon nanotubes *Nanoscale* 5 1411
- [39] Barone V, Hod O and Scuseria G E 2006 Electronic structure and stability of semiconducting graphene nanoribbons *Nano Lett.* 6 2748

- [40] Xia J and Jasti R 2012 Synthesis, characterization and crystal structure of [6]cycloparaphenylene *Angew. Chem., Int. Ed.* 51 2474
- [41] Bouilly D *et al* 2016 Single-molecule reaction chemistry in patterned nanowells *Nano Lett.* **16** 4679
- [42] Cao Q, Tersoff J, Farmer D B, Zhu Y and Han S-J 2017 Carbon nanotube transistors scaled to a 40-nanometer footprint *Science* **356** 1369
- [43] Saito R, Dresselhaus G and Dresselhaus M S 1998 *Physical Properties of Carbon Nanotubes* (London: Imperial College Press)